Technical University of Denmark

DTU

Imaging ultrafast excited state pathways in transition metal complexes by X-ray transient absorption and scattering using X-ray free electron laser source

Chen, Lin X; Shelby, Megan L; Lestrange, Patrick J; Jackson, Nicholas E; Haldrup, Kristoffer; Mara, Michael W; Stickrath, Andrew B; Zhu, Diling; Lemke, Henrik; Chollet, Matthieu; Hoffman, Brian M; Li, Xiaosong

DTU Library
Technical Information Center of Denmark

Imaging Ultrafast Excited State Pathways in Transition Metal Complexes by X-ray Transient Absorption and Scattering Using X-ray Free Electron Laser Source

Lin X. Chen[a,b], **Megan L. Shelby**[a,b], **Patrick J. Lestrange**[c], **Nicholas E. Jackson**[a,b], **Kristoffer Haldrup**[d], **Michael W. Mara**[b], **Andrew B. Stickrath**[a], **Diling Zhu**[e], **Henrik Lemke**[e], **Matthieu Chollet**[e], **Brian M. Hoffman**[b], and **Xiaosong Li**[c]

[a]Chemical Sciences and Engineering Division, Argonne National Laboratory, Lemont, Illinois, USA

[b]Department of Chemistry, Northwestern University, Evanston, Illinois, USA

[c]Department of Chemistry, University of Washington, Seattle, WA 98195, USA

[d]Physics Department, Technical University of Denmark, 2800 Kgs. Lyngby, Denmark

[e]LCLS, SLAC National Laboratory, Menlo Park, California 94025, USA

Abstract

This report will describe our recent studies of transition metal complex structural dynamics on the fs and ps time scales using an X-ray free electron laser source, Linac Coherent Light Source (LCLS). Ultrafast XANES spectra at the Ni K-edge of nickel(II) tetramesitylporphyrin (NiTMP) were successfully measured for optically excited state at a timescale from 100 fs to 50 ps, providing insight into its sub-ps electronic and structural relaxation processes. Importantly, a transient reduced state Ni(I) (π, $3d_{x2-y2}$) electronic state is captured through the interpretation of a short-lived excited state absorption on the low-energy shoulder of the edge, which is aided by the computation of X-ray transitions for postulated excited electronic states. The observed and computed inner shell to valence orbital transition energies demonstrate and quantify the influence of electronic configuration on specific metal orbital energies. A strong influence of the valence orbital occupation on the inner shell orbital energies indicates that one should not use the transition energy from 1s to other orbitals to draw conclusions about the d-orbital energies. For photocatalysis, a transient electronic configuration could influence d-orbital energies up to a few eV and any attempt to steer the reaction pathway should account for this to ensure that external energies can be used optimally in driving desirable processes. NiTMP structural evolution and the influence of the porphyrin macrocycle conformation on relaxation kinetics can be likewise inferred from this study.

Introduction

Transition metal complexes (TMCs) have been used broadly in photochemistry, especially in solar energy conversion processes[1–3] based on their versatility in light absorption, excited state redox properties as well as chemical tunability. One of the important criteria to determine if a TMC is suitable for solar energy conversion applications is the excited state

lifetime, often the triplet state lifetime, while the excited states before thermalization with short lifetimes are not fully explored. Historically, quantum mechanical calculations on TMCs were limited which also hindered our understanding of the unthermalized and relatively short-lived excited state TMCs as well as their applications. An active frontier in solar energy research is in search of low cost TMCs from the first row transition metals to replace those of high cost and relatively rare noble metal elements in many applications.[4–6] Recent studies have shown that some singlet excited state TMCs with picosecond lifetimes could be applied to useful to solar energy conversion processes if the charge separation/injection processes are fast enough to compete with other excited state decay pathways.[6–9] X-ray transient absorption (XTA) spectroscopy using synchrotron sources with approximately 100 ps time resolution has enhanced our understanding of TMS excited state structural dynamics significantly in the past two decades,[10–18] but many TMC excited state lifetimes are even shorter than 100 ps, which requires shorter pulsed X-ray sources, such as the X-ray Free electron lasers (XFELs) to study in addition to commonly used ultrafast laser spectroscopic methods. We have seen so far several examples of XTA from the new sources[9, 19–28] and expect many exciting results will come from these X-ray sources as well as table top X-ray sources with high harmonic generation with femtosecond time resolution in coming years.

Here we report our recent studies of TMS structural dynamics using an XFEL source, the Linac Coherent Light Source (LCLS). Compared to synchrotron sources, X-ray absorption spectroscopic measurements face new challenges due to the limited spectral range accessible to cover extended X-ray fine structure (EXAFS) region. Currently, the X-ray absorption measurements rely on the spectral fluctuation of self-amplified spontaneous emission (SASE) process of the source, which, depending on the energy, can cover 40 – 50 eV range near a central energy at the LCLS, sufficient for obtaining X-ray absorption near edge structure (XANES) spectra and X-ray emission (XES) spectra as shown in the literature. Therefore, the current femtosecond X-ray spectroscopy is focused on resolving excited state electronic structure while the nuclear geometry information is largely obtained by wide angle solution X-ray scattering.

Using this state-of-the-art source, we have obtained a number of XANES spectra at the Ni K-edge of nickel(II) tetramesitylporphyrin (NiTMP) and at Cu K-edge of copper(I) bis-dimethyl-phenanthroline ($[Cu(dmp)_2]^+$ in dilute solutions on a timescale from 100 fs to 50 ps, providing insight into their sub-picosecond electronic and structural relaxation processes. We mainly present here the results on NiTMP and highlight the discovery of a transient reduced state Ni(I) (π, $3d_{x2-y2}$) electronic state that was only be captured through with the femtosecond time resolution at the LCLS. Moreover, quantum mechanical calculations were carried out for both structures of the valence excited state and inner shell transitions which can be used to interpret our observed experimental results and gain insightful information on the electronic structures of the excited state as well as the interplays between energy levels of molecular orbitals with nuclear geometry changes. The observed and computed inner shell to valence orbital transition energies demonstrate and quantify the influence of electronic configuration on specific metal orbital energies. A strong influence of the valence orbital occupation on the inner shell orbital energies indicates that one should not use the transition energy from 1s to other orbitals to draw conclusions about the d-orbital energies.

These studies have brought new insights into electron and nuclear motions as the result of the light excitation. The information obtained here will help in designing new TMC based artificial photosynthetic systems, such as photocatalysts for solar fuel generation.

Results and discussion

The results from experimental measurements and calculations described below will here establish the NiTMP excited state kinetic scheme of Figure 1 and provide insight into how the evolving nuclear structure and electronic structure are interrelated as this decay occurs. This study allows us to capture the electronic configuration of the short-lived Ni(I) T′ state on the sub-ps timescale. The combined experimental and computational results that describe electronic transitions involving the inner shell electrons enables us to characterize properties that are not directly measureable using other ultrafast methods.

1. Excited State Pathways on Ultrafast Time Scales

NiTMP in solution has been chosen because it represents metalloporphyrins with open-shell transition metals whose excited states are short-lived and poorly understood due to the coupling between the molecular orbitals (MOs) involved in the initial (π, π*) excited state with metal d electron dominant MOs involved in light-activated redox reactions.[29] In our previous studies as well as others[30–36] using both optical and X-ray transient absorption spectroscopies, the excited state decay kinetics of NiTMP can be outlined by Figure 1.

Briefly, the electronic configuration of Ni(II) ($3d^8$) in a nearly square-planar ground state S_0 has an vacant $3d_{x2-y2}$ MO and a fully occupied $3d_{z2}$ MO.[37] The $S_0 \rightarrow S_1$ transitions in NiTMP can be induced by $\pi \rightarrow \pi$* transition at the Q-band centered at 530 nm. Within 300 fs of the excitation, S_1 is believed to convert, through energy transfer to an intermediate state T′ that then undergoes vibrational relaxation in less than 20 ps to a relaxed singlet or triplet state, T with a presumed $^{1,3}(3d_{x2-y2}, 3d_{z2})$ configuration,[38] where $3d_{x2-y2}$ and $3d_{z2}$ MOs are each singly occupied with an unsolved spin state.[39–42] The T $\rightarrow$ S_0 transition takes place with a time constant of ~200 ps. The electronic configurations of these excited states have been assigned largely according to computational results that describe charge-transfer states of transition metalloporphyrins with unfilled d orbitals.[43] Using the Advanced Photon Source (APS), a synchrotron source at Argonne National Laboratory, we previously carried out XTA measurements for NiTMP where the Ni-N bond elongation and porphyrin planarization at the T state were determined. The identity of the T′ state, however, remained to be unknown then. The previous study also identified the electronic configuration at the T state with single occupation in the two highest energy 3d MOs, $3d_{x2-y2}$, $3d_{z2}$.

From the LCLS results, Figure 2 displays the time evolution of the NiTMP XANES spectra as a function of the delay time between the laser pump pulse and X-ray probe pulse, ranging from −5 ps to 100 ps covering the time window that the synchrotron studies could not access. As shown in Figure 2, the ground state XANES spectrum collected at −5 ps time delay and the T state XANES at 100 ps time delay are largely the same as those obtained previously shown in the inset of Figure 2A.[10, 44] These peaks are assigned to the 1s $\rightarrow$ $4p_z$ transition.[45] Spectral features at 8351 eV are contributions from multiple scattering resonances and transitions from Ni 1s to $4p_x$ and $4p_y$ orbitals hybridized with porphyrin N

2s orbitals. In the pre-edge region from 8330 to 8336 eV are the weak quadrupole-allowed $1s \rightarrow 3d$ transitions, which directly probe the vacant the 3d electronic occupations,[46] according to the Ni coordination geometry and electronic state. Although the 4p MOs are not directly populated by valence transitions in our experiment, the energies induce $1s \rightarrow 4p$ transition are indicators for structural changes in the complex due to the correlations of the sensitivity of the TMC MOs to the geometry as observed in many complexes from the static XANES spectra.

The excited pathways $S_0 \rightarrow S_1 \rightarrow T' \rightarrow T$ transformation kinetics are extracted by analyzing the time dependent signal intensity in the difference spectra (Figure 2B) at three distinctive energies (shown by dashed vertical lines) at which assigned spectral features as afore mentioned can be followed. The peak position of the $1s \rightarrow 4p_z$ transition for the S_0 state at 8339.2 eV clearly shifts to 8340.8 eV, which are the same as in the synchrotron results within the experimental error. Notice that the relative peak heights at 8339 eV in the S_0 state spectrum and at 8341 eV in the T state are different due to compositions of the ground state contribution. The ground state contribution has been removed from the synchrotron spectrum for the T state (red curve in the inset of Figure 2A), while it remains in the LCLS spectra due to the difficulty to resolve sequential kinetics within a few picosecond after the excitation and distinguish the spectral difference from more than two states. In comparison, the synchrotron data with ~100-ps time resolution only involve two states, S_0 and T with the contributions from S_1 and T' neglected because they cannot be resolved and have minimal contribution beyond a few picoseconds delay. In the white line region, a peak feature shifts from 8359 eV to 8353 eV. While the $\sigma^*_{x,y}$ orbitals should shift to lower energy in the excited state as the Ni-N distances expand and the hybridization between the Ni $4p_{x,y}$ and Ni 2s orbitals is weakened,[47] the $4p_z$ transition blue shift cannot be explained initially because this MO should have minimal influence for the valence transitions considered here induced by the laser excitation because main structural changes as observed in previous synchrotron results are Ni-N bond expansion in the x-y plane.

A different view from the difference spectra in Figure 2B is presented in a contour plot in Figure 3. A transient feature at 8337 eV rises within ~100 fs of the pump pulse, peaks to its maximum amplitude in 400 – 800 fs, and disappears within 2 ps (see the orange patch). From then on, the XANES difference reflects an increasing population of T state that rises to its maximum within ~ 10 ps after the excitation.

The presence of this short-lived T' state can also be visualized by the time evolution of the $1s \rightarrow 4p_z$ peak from the ground state to the T state by comparing the kinetics of the bleach recovery of the ground state $1s \rightarrow 4p_z$ peak and the rise of the corresponding peak as the T state is generated. At the first glance the ground state depletion proceeds with a time constant of <1 ps, while the growth of the T state seems to have a rapid rise within ~200 fs and then a slower rise to the maximum peak height. The apparent kinetics seems to be against a common sense that the ground state depletion must be faster than other processes. Other dynamic spectral features on the same timescale include an apparent delay between the rise of the white line peak feature at 8353 eV, which is an indication of the Ni-N bond elongation as seen in the T state, and the rise of the $1s \rightarrow 4p_z$ the T state associated peak. Although at the high energy boundary of the XANES spectrum the X-ray photon flux drops,

resulting in noiser difference spectra, a growth of this feature in about 2 ps is clearly observed, suggesting a nuclear geometry change, most likely the Ni-N bond expansion due to the electronic configuration changes. The complication of a sequential kinetics and limited spectral region accessible prompted us to examine the kinetics beyond what appear in the time dependent signals at three energies mentioned above.

2. The Sequential Excited State Decay Kinetics

Averaged traces at the three characteristic energies were globally fit to a sequential kinetics model below:

$$S_1 \xrightarrow{k_1} T_1' \xrightarrow{k_2} T_1 \xrightarrow{k_3} S_0 \quad (1)$$
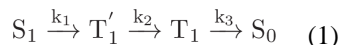
where k_i ($i = 1 - 3$) is the rate constant and its inverse $1/k_i$ is τ_i, the time constant for the i-th step of the reaction. The sequential kinetics for each species therefore can be expressed by the Equation (2) below:

$$
\begin{aligned}
[S_1(t)] &= [S_1(0)]e^{-k_1 t} \\
[T_1'(t)] &= \frac{k_1[S_1(0)]}{k_2 - k_1}\left[e^{-k_1 t} - e^{-k_2 t}\right] \\
[T_1(t)] &= \left[\frac{k_1 k_2 [S_1(0)]}{(k_2 - k_1)(k_3 - k_1)}\right]e^{-k_1 t} + \left[\frac{k_1 k_2 [S_1(0)]}{(k_1 - k_2)(k_3 - k_2)}\right]e^{-k_2 t} + \left[\frac{k_1 k_2 [S_1(0)]}{(k_3 - k_1)(k_2 - k_3)}\right]e^{-k_3 t} \\
[S_0(t)] &= [S_1(0)]\left\{1 - \frac{k_2 k_3 e^{-k_1 t}}{(k_2 - k_1)(k_3 - k_1)} - \frac{k_1 k_3 e^{-k_2 t}}{(k_1 - k_2)(k_3 - k_2)} - \frac{k_1 k_2 e^{-k_3 t}}{(k_3 - k_1)(k_3 - k_2)}\right]
\end{aligned}
\quad (2)
$$

The signals at different energies can therefore be described as Equation (3):

$$A_{total}(E, t) = \sum_{i=0}^{3} A_i(E) P_i(t) \quad (3)$$

where i is the index of the states, $i = 0 - 3$, corresponding to S_0, S_1, T', and T states, $A_i(E)$ is the relative absorption of the ith state at E, and $P_i(t)$ is the population of ith state at t. The relative absorption of the ground state S_0, $A_0(E)$ and that of the T state, $A_3(E)$ were obtained from XANES spectra at time delays with only the S_0 and T states present, which enables the T spectrum to be extracted by subtracting a fraction of the S_0 state contribution. The relative absorption $A_1(E)$ of the S_1 state is assumed to be identical to that of $A_0(E)$ because the (π, π^*) excitation is confined only on the macrocycle with very little effect on Ni. $A_2(E)$ for the T' state was treated as a variable during the fits. A_{total} was then convoluted with a Gaussian instrument response function (IRF) of ~300 fs due to the time drift of X-ray pulses. The data can be well-described by the kinetics scheme in Equation (1) and the spectral contributions in Equation (2) with three time constants, 1.0 ps, 0.08 ps, and a much longer one beyond the experimental time window. This long time constant, based on the previous studies, is ~200 ps assigned as the lifetime of the T state.[44, 48] Because $A_2(E)$ (Equation 2) is treated as a fitting variable, the assignment of 1.0 ps and 0.08 ps components to τ_1 and τ_2 is interchangeable in Equation (2). The two alternative assignments of τ_1 and τ_2 can be distinguished by taking into account of the T' absorption signals. With $\tau_1 = 1.0$ ps and $\tau_2 =$

0.08 ps, it requires T′ to have a much stronger signal than the ground state at 8337 eV and little population accumulation. When $\tau_1 = 0.08$ ps and $\tau_2 = 1.0$ ps, the rise of T will be much slower than observed in the experiment. The two scenarios can be distinguished based on the T′ signal amplitude at 8337 eV, and the first alternative is preferred in order to fit the observed kinetics. The kinetics for the formation and decay of T′ by apparent rise and decay can be easily misinterpreted as a sub-ps rise and a few ps decay while the true kinetics can be characterized by so called reverse kinetics where the decay is much faster than the rise. The errors for τ_1 and τ_2 are defined by 0.5fwhm of the IRF at ~0.15 ps, while the above results are best fit in the global analysis. The IRF has been improved at the XPP station recently to be sub-100 fs, but it was not completely implemented at time of our experiment.

Although the global fitting of kinetic traces at multiple X-ray photon energies can assist us to obtain rate constants for the sequential kinetics in Equation (2), the relative contributions from the species the XANES signals could only be confidently determined with the assignment of the difference XANES spectral feature at the $1s \rightarrow 4p_z$ transition peak of the T′ state. The global fitting under a kinetic scheme obtained from ultrafast optical transient absorption as well as the spectral assignments in terms of the inner shell to valent orbital transition energies from the calculations (shown below) are required to extract the true kinetics and capture the unknown species. The global fitting at three X-ray photon energies shows that while T′ has a small contribution to the total signal, its formation and decay lifetimes have a dramatic impact on the XAS signal kinetics. Although the kinetics of the T′ state absorption initially appear to be the result of an ultrafast generation rate $(\tau_1)^{-1}$ and a relatively slow decay rate $(\tau_2)^{-1}$ of the T′ species, the T′ *population* evolution can be described by the integrated rate law in Equation (2).

Relaxation through a charge transfer (CT) state that produces a transient Ni(I) intermediate has been previously hypothesized based on double-excitation optical methods.[49] Such a CT state has also been implicated as the route of excited porphyrin deactivation[50,51] by pump-probe photoelectron spectroscopy measurements which report fast time constants for the evolution of the NiOEP excited state absorption very similar to this work (100 fs and 1.2 ps). A short-lived T′ state is also compatible with previous work confirming the presence of the T state on the picosecond time scale,[52, 53] which depicted the S_1 relaxation process as a simultaneous transfer of the excitation from S_1 to T, and observed slower decay processes as vibrational cooling of a hot T state. During the first 10 ps after excitation, vibrational relaxation processes may also influence the XANES in subtle ways before the T state is fully thermalized. Nuclear movement during vibrational cooling will affect the 3d orbital energies, especially those involved in coordination to the porphyrin ring, which would be reflected in the dynamics of the $1s \rightarrow 3d$ transition region as general broadening of the 3d transitions in T. Such influence of the coordination geometry to the linewidth of the $1s \rightarrow 3d$ transition was also observed in the ground state with coexisting multiple conformers.[2] This may provide some explanation of the shape of the 3d transitions at 10 ps, although a full description of the relaxation processes in terms of nuclear movement requires additional measurement with more direct structurally sensitive techniques, such as extended X-ray absorption fine structure (EXAFS) or wide angle X-ray scattering (WAXS). In the past synchrotron XTA experiments, we normally dealt with only two species at two delay times, the ground state at negative delay before the laser pulse, and the excited state at a positive

delay with the laser excitation. Because the spectral feature of the ground state is known, its contribution can subtracted from the total signal to extract the excited state spectrum if the fraction of the remaining ground state is known. At the LCLS, as shown by Equation (3), the relative contributions of each species to the total signal vary as a function of the delay time, and a very good kinetic scheme as well as the spectral assignments will be required to extract the kinetics of each transient species in the excited state trajectory.

3 Ni 3d Electron Configuration Dynamics

The electronic configurations of Ni transient states can be captured by time evolution of the pre-edge features from quadrupole-allowed transitions from 1s to vacant 3d which provide directly the electronic configuration information of the vacant 3d orbitals. We have determined the pre-edge features for S_0, a single peak assigned to the $1s \rightarrow 3d_{x2-y2}$ transition arising from the Ni(II) $3d^8$ electronic configuration of $(3d_{z2})^2(3d_{x2-y2})^{0.4}$[44] Also determined were the pre-edge features for the T_1 state where the two peaks were assigned to the $1s \rightarrow 3d_{x2-y2}$ and $1s \rightarrow 3d_{z2}$ transitions respectively for the $(3d_{z2})^1(3d_{x2-y2})^1$ electronic configuration. In the LCLS experiment, the time evolution of the pre-edge features were captured in a much higher time resolution as shown in Figure 5. Before the laser excitation, the pre-edge of S_0 again shows a single peak as we observed before. At t = 1 ps, the magnitude of this peak is diminished and slightly red shifted, while by t = 10 ps the pre-edge features are significantly broadened with some intensity growing in at lower energy. At t = 50 ps, the double peak features for T_1 are observed again. Due to the weak signals from the pre-edge, we could only take a few discrete time points, which may have missed the rise of the double peak feature, while we can still suggest that the double singly occupancy at $3d_{x2-y2}$ and $3d_{z2}$ could have appeared between t = 10 – 50 ps. The absence of sharp split peaks by 1 ps is consistent with the presence of intermediate T'_1 at this delay time. The interesting part of the result is the visualization of the transient Ni(I) species in T'_1 an intramolecular charge transfer state where the electronic occupation is $(3d_{z2})^2(3d_{x2-y2})^1$ from the relaxation of the $S_1(\pi,\pi^*)$ state via charge transfer to Ni(II). The partial occupation of the $3d_{x2-y2}$ orbital diminishes the probability of the $1s \rightarrow 3d_{x2-y2}$ transition. The T' decay to T_1 is a second charge transfer event, filling the hole in the π orbital and resulting in a Ni(II) d-centered excitation.

4. Excited State Electronic Structures of NiTMP from XANES and Calculations

Although one can obtain XANES spectral features for different transient states of NiTMP, the precise assignments of these features can be benefit from electronic structural calculations from which the XANES transition features can be obtained to compare with the experimental results. Although calculations for the ground state TMCs become relatively routine processes, the corresponding calculations for the valence excited state as well as the corresponding inner shell transitions are rare. DFT and TDDFT calculations identified possible electronic states participating in the relaxation pathway. Ground and excited state geometry optimizations of these potential intermediate electronic states provided their relative energies and structural characteristics as shown in Figure 6.

Using the optimized ground state geometry, the S_1 state Frank-Condon excitation energy is computed which is 2.31 eV above the ground state. Any intermediate states in the singlet

manifold should be rapidly populated. The TDDFT excited state geometry optimizations performed on the lowest lying singlet excited states found the lowest A state at 1.31 eV and the lowest B state at 1.81 eV. The lowest A singlet state, which possesses (π, $3d_{x2-y2}$) orbital character, is chosen as a point of probable intersystem crossing and triplet states computed using the geometry optimized in this lowest A state provides a probable candidate for the identity of T′ because it resides in the singlet manifold of the lowest energy state and its energy proximity of the singlet and triplet of (π, $3d_{x2-y2}$) character. The T′ state with a (π, d) configuration is identified with a $(3d_{z2})^2(3d_{x2-y2})^1$ configuration due to the observed XANES pre-edges.

Relaxed geometries for the ground, S_1, T′, and T states show significant differences in their structures, with the calculated Ni-N bond lengths of 1.94, 2.02 and 2.04 Å, respectively, and the macrocycle structure from a significant out-of-plane ruffling distortion to largely planar conformation. The Ni-N bond lengthening for the T state is very similar to the synchrotron results.[44, 54] Interestingly, the calculated Ni-N bond lengths for the T′ state are almost the same as the T state, suggesting a structural similarity between the geometry of the relaxed T′ and T states around the Ni centre.

In order to compute the XANES features based on the molecular structures and valence electronic configurations, a series of inner shell bound transitions were calculated using the solutions to the Self Consistent Field (SCF) equations that converge to at a higher energy than ground state solutions that have long been recognized as useful approximations to excited state wave functions.[55–57] In order to obtain these higher-energy SCF solutions, a set of natural transition orbitals (NTOs)[58] for the state of interest was first generated at the excited state geometry. The initial guess for the SCF density of this higher-energy solution was then formed by a HOMO-LUMO swap of the dominant NTOs. A second-order optimization scheme was then used to converge to the state of interest.[59] The XANES features for the intermediate states were calculated with ES-TDDFT. Due to the neglect of scalar and spin-orbit relativistic effects in this simulation, the calculated transitions are much lower in energy than the experimental results. However, it has been shown that these operators have little effect on relative transition energies[60] and uniform shifts are routinely applied to calculated XANES spectra to better compare transition energies with experimental data.[60–62] A uniform shift of 172 eV (~2% of the Ni K-edge energy) is applied to all calculated spectra and all transitions are convoluted with Gaussian functions to match experimental lineshapes; 2.2 and 1.8 eV FWHM for the $4p_z$ and 3d transitions respectively.

The electronic environment around the Ni remains essentially the same from S_0 to S_1, so little change is seen in the dominating 1s → $4p_z$ transition from the calculation. The observed blue-shift of the T 1s → $4p_z$ transition feature compared to S_0 is also reproduced in the calculation. More interestingly, a red shift for the 1s → $4p_z$ transition is produced from the calculation also as observed for the T′ state. The calculated results clearly identified the origin of these shifts. For the T′ state, the red-shift of its 1s → $4p_z$ transition peak, based on the calculated results (Table 1), is due to the energy rise of the 1s core level energy by about 2 eV, reducing the energy gap between 1s and $4p_z$ orbitals, while the $4p_z$ orbital energy only changes on the order of 0.1 eV. This could be due to the transient reduction of the Ni(II) to Ni(I) which gives rise of the red-shift at the edge. For the T state,

the blue shift of the 1s → $4p_z$ peak could also also originate from simultaneous lowering of the 1s core level energy by ~1.2 eV and the $4p_z$ energy level by < 0.2 eV to give rise to the blue shift by 1 eV compared to the experimental value of 1.5 eV, with the difference comparable to the energy resolution of the experiments. In addition, the calculations also successfully reproduced the trend of the 1s → 3d transitions with the expected 3d electronic configuration and nuclear geometry (not shown).

We can therefore conclude that the $4p_z$ transition energy is largely determined by the electronic state of the Ni, which is in line with the fact that the shift in the 1s energy dominates the observed shifts and that $4p_z$ has less interaction with ligand orbitals than other valence Ni orbitals.

5. What we have learned about interplay between electronic and nuclear structural changes in the excited state NiTMP?

The time scale in structural dynamics studies enabled by the LCLS allows us to directly probe transient metal orbital energies and occupancy as well as interplays of photoinduced electronic configuration changes and molecular orbital energies before excited state thermalization. While ultrafast optical transient absorption measurements can obtain kinetics of the S_1 state decay, optically dark metal centered electronic state, or metal centered orbital energy changes in the subsequent excited states are often elusive by these methods. This study has directly obtained energies of the transitions 1s → 3d and 1s → $4p_z$ in Ni for different electronic states from the experimental and computational studies which appears to be a key to extract the information regarding the interplays between electronic and nuclear movement in the excited state since the transient EXAFS is not currently available in the X-ray free electron source.

Moreover, only the comparison between the 1s to 3d and 4p transition energies obtained from XANES and calculated energies of these orbitals can provide the information about the origin of the transition energy changes and quantity the influence of the valence excitation and the energy level of the core orbital. The experimental results only could not identify the red-shift of 1s → $4p_z$ transition is an evidence of the T′ state formation and the evidence could be misinterpreted or missed entirely without the computation. With the assignment of T′ to Ni(I), T′ state formation can be understood as the intramolecular electron movement from the macrocycle to the metal center $3d_{x2-y2}$ orbital, causing greater nuclear shielding and therefore a lower electron binding energy. The rise of the 1s orbital energy in turn reduces the 1s → $4p_z$ transition energy in the T′ state, analogous to the core-level shift seen in X-ray photoelectron spectroscopy (XPS)[63] and the effect of oxidation transition edge energies in previous XAS experiments.[64, 65] The 2 eV rise of the Ni 1s orbital energy due to the formation of Ni(I) and associated nuclear structural change reminds us that the energy of the core orbital can be affected by the valence excitation although only less than 0.1% respect to the core transition energy, it is sufficiently large to affect our interpretation of the XANES results.

The results reported here also provide direct information on the mutual influence between molecular orbitals associated with the metal center which has been difficult to obtain with other means. This red shift resulted from the formation of the transient Ni(I) is the first

direct observation of this intermediate state in this system. A strong influence of the valence orbital occupation on the inner shell orbital energies indicates that one should not use the transition energy from 1s to other orbitals to draw conclusions about the d-orbital energies. As calculated, only ~0.2 eV of the ~2 eV shift in the 1s $\rightarrow$ 4p$_z$ transition energy change is from the changes in the 4p$_z$ orbital from S$_0$ to T$'$. The blue shift in the 1s→4p$_z$ transition energy of the T state can again be attributed to a change in the repulsive potential felt by the core electrons due to more antibonding electrons with weaker interactions with the core. Consequently, this change reduces the repulsive potential felt by the Ni 1s electrons, lowering the 1s orbital energy, and increasing the energy gap for the the 1s $\rightarrow$ 4p$_z$ transition by 1.5 eV relative to that of the ground state. The identification by TDDFT of T$'$ as the lowest energy singlet as well as a state with a triplet state lying close in energy lends credence to the identification of T$'$ as a (π, d) state. The optimized geometries of the involved electronic states (Figure 6) provide insight into the behavior of the NiTMP structure in response to electronic changes and the subsequent energetic rearrangement of Ni orbitals.

Macrocycle expansion and flattening in the T state is explained based on the net movement of electron density from 3d$_{z2}$ to 3d$_{x2-y2}$ in the porphyrin plane destabilizing the Ni-N bonds, which leads to the bond elongation. Such an electronic movement makes the effective radius of Ni(II) larger than in the S$_0$ state and significantly removes the need for the non-planar distortion of the porphin to accommodate the unusually short Ni-N bond length. Interestingly, the calculated Ni-N bonds in the Ni(I) of the T$'$ state already have the majority of the lengthening of the Ni-N bond, suggesting that even with only one additional electron on the 3d$_{x2-y2}$ orbital could cause substantial nuclear geometry change. This is the direct evidence for the interplays between the electronic and nuclear structures of a TMC.

In the ground state, Ni porphyrins have a low barrier to interconversion between various distorted conformers of the macrocycle,[66, 67] relative broadness of the 1s $\rightarrow$ 3d$_{x2-y2}$ transition peak.[54] The lowest in energy of these conformers based on our calculations is a ruffled geometry. Out-of-plane distortions are structural factors that influence electronic state energies mainly through the destabilization of the π and 3d$_{x2-y2}$ orbitals, an effect that when taken to a greater extreme in substituted Ni phthalocyanines (Pc) begins to lead to *longer* CT state lifetimes. The octabutoxy substituted Ni(II)Pc have been described as having long-lived LMCT states with lifetimes in the hundreds of picoseconds.[68, 69] Based on our studies on Ni(II)TMP with preferred planar structure to accommodate the Ni(I) species, one can relate the results from Ni(II)Pc to suggest using planar Ni(II) species as potential reducing catalysts, even though such correlation remains to be investigated in the future.

Experimental

1. Ultrafast XANES Spectroscopy

Ultrafast XANES spectra were collected for an 8 mM solution of NiTMP in toluene at the X-ray Pump-Probe (XPP) station of the LCLS[70] using a similar experimental configuration as previous XANES measurements at XPP.[19] The sample solution was delivered as a flat 100 μm thick liquid jet where the laser and X-ray overlap nearly collinearly in a nitrogen filled chamber. The "pump-probe" cycle of was at 120 Hz repetition rate. The pump laser

pulses are from the output of an optical parametric amplifier (OPA) at 527 nm with a pulse duration of 50 fs (FWHM). The laser pulse energy at the sample was between 15 and 18 μJ with a spot size of ~0.1 mm diameter. Ni K-edge (8333 eV) XANES spectra were collected by scanning a Si(111) double crystal X-ray monochromator across the XFEL SASE bandwidth. The ~50 fs pulse duration X-ray probe pulses have significant bunch-to-bunch spectral and temporal fluctuations, resulting in a time-integrated energy bandwidth of ~50 eV at the Ni K-edge. The monochromatic X-ray beam was focused to a ~0.1 mm diameter spot at the sample. To obtain the kinetics at a specific energy, scans of the pump-probe delay were performed at the fixed photon energies as described in the results. For both scan types, the XANES signal was collected with two seconds integration time and a total of 240 single pulses were used at each energy step.

XANES spectra via Ni K_α X-ray fluorescence were collected using two solid state passivated implanted planar silicon (PIPS) point detectors (Canberra, Inc.) each equipped with a set of Z-1 filter and soller slits to minimized the elastic scattering signals. The raw data from XANES scans were smoothed with the locally weighted regression method.

To account for timing jitter in the X-ray pulses, individual shots were re-binned in time for time delay scans according to up-stream diagnostic RF cavities ("phase cavities") that record the average electron bunch arrival time. This signal is used to account for the long-time drift in the average pulse arrival time and replaces and enhances the overall time resolution of the experiments. After phase cavity re-binning, the time resolution of the experiment was reduced from an estimated 400 fs to 300 fs based on the FWHM of the Gaussian instrument response function (IRF) obtained as a fitted variable in the fits of the time delay scans.

To obtain kinetics for the NiTMP XANES evolution, signals at a chosen X-ray photon energy were collected as a function of the pump-probe delay time as shown in Figure 4. These kinetic traces were fit globally to a sequential kinetic scheme in Equation (1). Based on this scheme, the relative populations of each species as a function of the delay time were simulated by numerical integration of a set of differential equations shown in Equation (2). These are the differential rate expressions for each species included in the kinetic scheme. τ_1, τ_2, and τ_3 are assigned to the first second and third steps in Equation (1) respectively. These components were weighted by their relative absorption at each energy and the total simulated kinetic traces were fit to the experimental traces using a non-linear least squares method to obtain time constants for each step as shown in Equation (3) as described earlier.

2. Electronic Structure Calculations

To understand the overall electronic and structural evolution of the NiTMP excited states and to ascertain how changes in the electronic and nuclear structure as the molecule relaxes are reflected in the experimentally observed XTA signals, each electronic state in the proposed mechanism (Figure 1) was modeled separately. Initial DFT and TDDFT calculations using the BP86 functional were employed to probe the basic orbital structure of NiTMP and its excited states using the ADF package (ADF2013.01[71, 72]). A double-ζ polarized (DZP) basis set was used for the description of C, N, and H atoms, and a triple-ζ polarized (TZP) basis set was used to describe the atomic orbitals of Ni. This combination of functional and basis set has previously described the orbital structure of a related Ni compound with high

accuracy.[73] Subsequently, the geometries of the ground and each intermediate excited state were optimized with the BP86 functional[74–76] and the 6-31G(d) basis set[77, 78] using a development version of the Gaussian software package.[76] The X-ray absorption was calculated with energy-specific TDDFT (ES-TDDFT)[79, 80] using the PBE1PBE and Ahlrichs' def2-TZVP basis set[81] with diffuse functions on the nickel atom.[82–84] For all calculations of X-ray absorption spectra, the mesityl groups on the porphyrin have been replaced with methyl groups to reduce computational cost.

Conclusions

Ultrafast excited state pathways for an open shell metalloporphyrin Ni(II)TMP are obtained based on XANES spectra at the Ni K-edge with ~100 fs time resolution at the LCLS, providing insight into its ultrafast electronic and structural relaxation processes. Importantly, a transient Ni(I) (π, d) electronic state (T$'$) is captured as an intermediate from analyzing the spectral data and quantum mechanical calculations.

The observed and computed inner shell-to-valence orbital transition energies demonstrate and quantify the influence of electronic configuration on specific metal orbital energies. The strong influence of the valence orbital occupation on the inner shell orbital energies indicates that one should not use the transition energy from 1s alone to draw conclusions about the d-orbital energies of different states. A transient electronic configuration could influence d-orbital energies up to a few eV and any potential photocatalytic application should account for this to ensure that energy levels are well matched and that the photoexcitation can be used optimally in driving desirable processes.

NiTMP structural dynamics have been deduced from DFT optimized geometries and structurally sensitive features in the Ni K-edge XANES. The influence of the porphyrin macrocycle conformation on relaxation kinetics may be significant enough to affect the kinetics that govern the limited population accumulation of Ni(I). The short lifetime of the T$'$ state and the delay of the nuclear rearrangement to a longer Ni-N bond length and flattened macrocycle with respect to its formation suggests the still-ruffled macrocycle expedites T$'$ decay.

Acknowledgments

References

1. Balzani V, Credi A, Venturi M. Coord Chem Rev. 1998; 171:3–16.

2. Meyer TJ. Acc Chem Res. 1989; 22:163–170.

3. Gray HB. Nat Chem. 2009; 1:7–7. [PubMed: 21378780]

4. Smeigh AL, McCusker JK. Ultrafast Phenomena. 2006:273–275.

5. Castellano FN, Ruthkosky M, Meyer GJ. Inorg Chem. 1995; 34:3–4.

6. Huang J, Buyukcakir O, Mara MW, Coskun A, Dimitrijevic NM, Barin G, Kokhan O, Stickrath AB, Ruppert R, Tiede DM, Stoddart JF, Sauvage JP, Chen LX. Angew Chem Intl Ed. 2012; 51:12711–12715.

7. Ferrere S, Zaban A, Gregg BA. J Phys Chem B. 1997; 101:4490–4493.

8. Jamula LL, Brown AM, Guo D, McCusker JK. Inorg Chem. 2014; 53:15–17. [PubMed: 24341550]

9. Mara MW, Bowman DN, Buyukcakir O, Shelby ML, Haldrup K, Huang J, Harpham MR, Stickrath AB, Zhang X, Stoddart JF, Coskun A, Jakubikova E, Chen LX. J Am Chem Soc. 2015; 137:9670–9684. [PubMed: 26154849]

10. Chen LX, Jäger WJH, Jennings G, Gosztola DJ, Munkholm A, Hessler JP. Science. 2001; 292:262–264. [PubMed: 11303096]

11. Chen LX. Angew Chemie, Intl Ed. 2004; 43:2886–2905.

12. Chen LX. Ann l Rev Phys Chem. 2005; 56:221–254.

13. Chen LX, Zhang X. J Phys Chem Lett. 2013; 4:4000–4013.

14. Chen LX, Zhang X, Shelby ML. Chem Sci. 2014; 5:4136–4152.

15. Saes M, Bressler C, Abela R, Grolimund D, Johnson SL, Heimann PA, Chergui M. Physical Review Letters. 2003; 90:047403/047401–047403/047404. [PubMed: 12570459]

16. Bressler C, Chergui M. Chem Rev. 2004; 104:1781–1812. [PubMed: 15080712]

17. Bressler C, Milne C, Pham VT, ElNahhas A, van der Veen RM, Gawelda W, Johnson S, Beaud P, Grolimund D, Kaiser M, Borca CN, Ingold G, Abela R, Chergui M. Science. 2009; 323:489–492. [PubMed: 19074309]

18. Chergui M. Acta Crystallographica Section A. 2010; 66:229–239.

19. Lemke HT, Bressler C, Chen LX, Fritz DM, Gaffney KJ, Galler A, Gawelda W, Haldrup K, Hartsock RW, Ihee H, Kim J, Kim KH, Lee JH, Nielsen MM, Stickrath AB, Zhang WK, Zhu DL, Cammarata M. J Phys Chem A. 2013; 117:735–740. [PubMed: 23281652]

20. Chollet M, Alonso-Mori R, Cammarata M, Damiani D, Defever J, Delor JT, Feng Y, Glownia JM, Langton JB, Nelson S, Ramsey K, Robert A, Sikorski M, Song S, Stefanescu D, Srinivasan V, Zhu D, Lemke HT, Fritz DM. J Sync Rad. 2015; 22:503–507.

21. Colletier JP, Sliwa M, Gallat FX, Sugahara M, Guillon V, Schiro G, Coquelle N, Woodhouse J, Roux L, Gotthard G, Royant A, Uriarte LM, Ruckebusch C, Joti Y, Byrdin M, Mizohata E, Nango E, Tanaka T, Tono K, Yabashi M, Adam V, Cammarata M, Schlichting I, Bourgeois D, Weik M. J Phys Chem Lett. 2016; 7:882–887. [PubMed: 26866390]

22. Higley DJ, Hirsch K, Dakovski GL, Jal E, Yuan E, Tianmin L, Lutman AA, MacArthur JP, Arenholz E, Zhao C, Coslovich G, Denes P, Granitzka PW, Hart P, Hoffmann MC, Joseph J, Le Guyader L, Mitra A, Moeller S, Ohldag H, Seaberg M, Shafer P, Stohr J, Tsukamoto A, Nuhn HD, Reid AH, Durr HA, Schlotter WF. Rev Sci Instr. 2016; 87:033110–5.

23. Katayama T, Inubushi Y, Obara Y, Sato T, Togashi T, Tono K, Hatsui T, Kameshima T, Bhattacharya A, Ogi Y, Kurahashi N, Misawa K, Suzuki T, Yabashi M. Appl Phys Lett. 2013; 103:131105.

24. Kern J, Tran R, Alonso-Mori R, Koroidov S, Echols N, Hattne J, Ibrahim M, Gul S, Laksmono H, Sierra RG, Gildea RJ, Han G, Hellmich J, Lassalle-Kaiser B, Chatterjee R, Brewster AS, Stan CA, Gloeckner C, Lampe A, DiFiore D, Milathianaki D, Fry AR, Seibert MM, Koglin JE, Gallo E, Uhlig J, Sokaras D, Weng TC, Zwart PH, Skinner DE, Bogan MJ, Messerschmidt M, Glatzel P, Williams GJ, Boutet S, Adams PD, Zouni A, Messinger J, Sauter NK, Bergmann U, Yano J, Yachandra VK. Nat Comm. 2014; 5:4371.

25. Kim J, Kim KH, Oang KY, Lee JH, Hong K, Cho H, Huse N, Schoenlein RW, Kim TK, Ihee H. Chem Comm. 2016; 52:3734–3749. [PubMed: 26785280]

26. Obara Y, Katayama T, Ogi Y, Suzuki T, Kurahashi N, Karashima S, Chiba Y, Isokawa Y, Togashi T, Inubushi Y, Yabashi M, Suzuki T, Misawa K. Opt Exp. 2014; 22:1105–1113.

27. Ogi Y, Obara Y, Katayama T, Suzuki YI, Liu SY, Bartlett NCM, Kurahashi N, Karashima S, Togashi T, Inubushi Y, Ogawa K, Owada S, Rubesova M, Yabashi M, Misawa K, Slavicek P, Suzuki T. Struc Dynamics. 2015; 2:034901.

28. Uemura Y, Kido D, Wakisaka Y, Uehara H, Ohba T, Niwa Y, Nozawa S, Sato T, Ichiyanagi K, Fukaya R, Adachi S-i, Katayama T, Togashi T, Owada S, Ogawa K, Yabashi M, Hatada K, Takakusagi S, Yokoyama T, Ohtani B, Asakura K. Angew Chem Intl Ed. 2016; 55:1364–1367.

29. Kalyanasundaram, K. Photochemistry of Polypyridine and Porphyrin Complexes. Academic Press; London: 1992.

30. Chen LX, Zhang X, Wasinger EC, Attenkofer K, Jennings G, Muresan AZ, Lindsey JS. J Am Chem Soc. 2007; 129:9616–9618. [PubMed: 17636917]

31. Chen LX, Zhang X, Wasinger EC, Lockard JV, Stickrath AB, Mara MW, Attenkofer K, Jennings G, Smolentsev G, Soldatov A. Chemical Science. 2010; 1:642.

32. Kim D, Holten D. Chem Phys Lett. 1983; 98:584–589.

33. Rodriguez J, Holten D. J Chem Phys. 1990; 92:5944–5950.

34. Zamyatin AV, Gusev AV, Rodgers MAJ. J Am Chem Soc. 2004; 126:15934–15935. [PubMed: 15584706]

35. Jentzen W, Unger E, Karvounis G, Shelnutt JA, Dreybrodt W, Schweitzer-Stenner R. J Phys Chem. 1996; 100:14184–14191.

36. Drain CM, Gentemann S, Roberts JA, Nelson NY, Medforth CJ, Jia S, Simpson MC, Smith KM, Fajer J, Shelnutt JA, Holten D. J Am Chem Soc. 1998; 120:3781–3791.

37. Ballhausen. Introduction to Ligand Field Theory. McGraw-Hill; New York: 1962.

38. Zhang X, Wasinger EC, Muresan AZ, Attenkofer K, Jennings G, Lindsey JS, Chen LX. J Phys Chem A. 2007; 111:11736–11742. [PubMed: 17966996]

39. Kim D, Kirmaier C, Holten D. Chem Phys. 1983; 75:305–322.

40. Rodriguez J, Holten D. J Chem Phys. 1989; 91:3525–3531.

41. Gentemann S, Nelson NY, Jaquinod L, Nurco DJ, Leung SH, Medforth CJ, Smith KM, Fajer J, Holten D. J Phys Chem B. 1997; 101:1247–1254.

42. Eom HS, Jeoung SC, Kim D, Ha JH, Kim YR. J Phys Chem A. 1997; 101:3661–3669.

43. Zamyatin AV, Gusev AV, Rodgers MAJ. J Am Chem Soc. 2004; 126:15934–15935. [PubMed: 15584706]

44. Chen LX, Zhang X, Wasinger EC, Attenkofer K, Jennings G, Muresan A, Lindsey Jonathan S. J Am Chem Soc. 2007; 129:9616–9618. [PubMed: 17636917]

45. Kau LS, Spira-Solomon DJ, Penner-Hahn JE, Hodgson KO, Solomon EI. J Am Chem Soc. 1987; 109:6433–6442.

46. Westre TE, Kennepohl P, DeWitt JG, Hedman B, Hodgson KO, Solomon EI. J Am Chem Soc. 1997; 119:6297–6314.

47. Campbell L, Tanaka S, Mukamel S. Chem Phys. 2004; 299:225–231.

48. Zhang XY, Wasinger EC, Muresan AZ, Attenkofer K, Jennings G, Lindsey JS, Chen LX. J Phys Chem A. 2007; 111:11736–11742. [PubMed: 17966996]

49. Zamyatin AV, Gusev AV, Rodgers MAJ. J Am Chem Soc. 2004; 126:15934–15935. [PubMed: 15584706]

50. Ha-Thi MH, Shafizadeh N, Poisson L, Soep B. Phys Chem Chem Phys. 2010; 12:14985. [PubMed: 20949219]

51. Sorgues S, Poisson L, Raffael K, Krim L, Soep B, Shafizadeh N. J Chem Phys. 2006; 124:114302–114310. [PubMed: 16555883]

52. Mizutani Y, Uesugi Y, Kitagawa T. J Chem Phys. 1999; 111:8950–8962.

53. Rodriguez J, Holten D. J Chem Phys. 1989; 91:3525–3531.

54. Chen LX, Zhang X, Wasinger EC, Lockard JV, Stickrath AB, Mara MW, Attenkofer K, Jennings G, Smolentsev G, Soldatov A. Chem Sci. 2010:1.

55. Gilbert ATB, Besley NA, Gill PMW. J Phys Chem A. 2008; 112:13164–13171. [PubMed: 18729344]

56. Davidson ER. J Chem Phys. 1964; 41:656.

57. Peng B, Van Kuiken BE, Ding F, Li X. J Chem Theor Comput. 2013; 9:3933–3938.

58. Martin RL. J Chem Phys. 2003; 118:4775.

59. Bacskay GB. Chem Phys. 1981; 61:385–404.

60. DeBeer George S, Petrenko T, Neese F. Inorg Chem Acta. 2008; 361:965–972.

61. Besley NA, Asmuruf FA. Phys Chem Chem Phys. 2010; 12:12024. [PubMed: 20714478]

62. Fronzoni G, De Francesco R, Stener M. J Phys Chem B. 2005; 109:10332–10340. [PubMed: 16852252]

63. Fadley CS, Hagstrom SBM, Klein MP, Shirley DA. J Chem Phys. 1968; 48:3779–3794.

64. Sarangi R, DeBeer George S, Rudd DJ, Szilagyi RK, Ribas X, Rovira C, Almeida M, Hodgson KO, Hedman B, Solomon EI. J Am Chem Soc. 2007; 129:2316–2326. [PubMed: 17269767]

65. Gu W, Wang H, Wang K. Dalton Trans. 2014; 43:6406. [PubMed: 24604143]

66. Alden RG, Crawford BA, Doolen R, Ondrias MR, Shelnutt JA. J Am Chem Soc. 1989; 111:2070–2072.

67. Alden RG, Ondrias MR, Shelnutt JA. J Am Chem Soc. 1990; 112:691–697.

68. Balakrishnan G, Soldatova AV, Reid PJ, Spiro TG. J Am Chem Soc. 2014; 136:8746–8754. [PubMed: 24841906]

69. Drain CM, Gentemann S, Roberts JA, Nelson NY, Medforth CJ, Jia S, Simpson MC, Smith KM, Fajer J, Shelnutt JA, Holten D. J Am Chem Soc. 1998; 120:3781–3791.

70. Chollet M, Alonso-Mori R, Cammarata M, Damiani D, Defever J, Delor JT, Feng Y, Glownia JM, Langton JB, Nelson S, Ramsey K, Robert A, Sikorski M, Song S, Stefanescu D, Srinivasan V, Zhu D, Lemke HT, Fritz DM. J Sync Rad. 2015; 22:503–507.

71. Fonseca uGerra C, Snijders JG, te Velde G, Baerends EJ. Theor Chem Acc. 1998; 99:391–403.

72. te Velde G, Bickelhaupt FM, Baerends EJ, Fonseca Guerra C, van Gisbergen SJA, Snijders JG, Ziegler T. J Comput Chem. 2001; 22:931–967.

73. Patchkovskii S, Kozlowski PM, Zgierski MZ. J Chem Phys. 2004; 121:1317–1324. [PubMed: 15260674]

74. Becke AD. J Chem Phys. 1986; 84:4524.

75. Perdew J. Phys Rev B. 1986; 33:8822–8824.

76. Frisch MJ, Trucks GW, Schlegel HB, Scuseria GE, Robb MA, Cheeseman JR, Scalmani G, Barone V, Mennucci B, Petersson GA, Nakatsuji H, Caricato M, Li X, Hratchian HP, Izmaylov AF, Bloino J, Zheng G, Sonnenberg JL, Hada M, Ehara M, Toyota K, Fukuda R, Hasegawa J, Ishida M, Nakajima T, Honda Y, Kitao O, Nakai H, Vreven T, JAM, Peralta JE, Ogliaro F, Bearpark M, Heyd JJ, Brothers E, Kudin KN, Staroverov VN, Keith T, Kobayashi R, Normand J, Raghavachari K, Rendell A, Burant JC, Iyengar SS, Tomasi J, Cossi M, Rega N, Millam JM, Klene M, Knox JE, Cross JB, Bakken V, Adamo C, Jaramillo J, Gomperts R, Stratmann RE, Yazyev O, Austin AJ, Cammi R, Pomelli C, Ochterski JW, Martin RL, Morokuma K, Zakrzewski VG, Voth GA, Salvador P, Dannenberg JJ, Dapprich S, Daniels AD, Farkas O, Foresman JB, Ortiz JV, Cioslowski J, Fox DJ. Gaussian. 2010; 9

77. Rassolov VA, Pople JA, Ratner MA, Windus TL. J Chem Phys. 1998; 109:1223–1229.

78. Hariharan PC, Pople JA. Theor Chem Acc. 1973; 28:213–222.

79. Liang W, Fischer SA, Frisch MJ, Li X. J Chem Theor Comput. 2011; 7:3540–3547.

80. Lestrange PJ, Nguyen PD, Li X. J Chem Theor Comput. 2015 Submitted.

81. Weigend F, Ahlrichs R. Phys Chem Chem Phys. 2005; 7:3297. [PubMed: 16240044]

82. Rappoport D, Furche F. J Chem Phys. 2010; 133:134105. [PubMed: 20942521]

83. Schuchardt KL, Didier BT, Elsethagen T, Sun L, Gurumoorthi V, Chase J, Li J, Windus TL. J Chem Inf Model. 2007; 47:1045–1052. [PubMed: 17428029]

84. Feller D. J Comp Chem. 1996; 17:1571–1586.

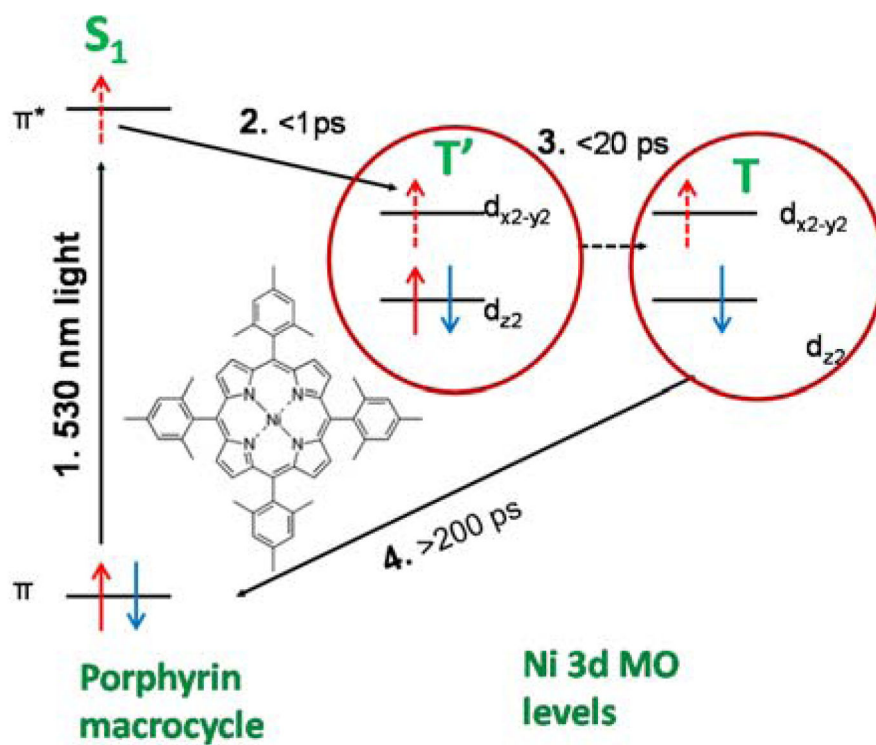**Figure 1.**
NiTMP excited state pathways and decay time constants obtained from optical transient absorption spectroscopy.
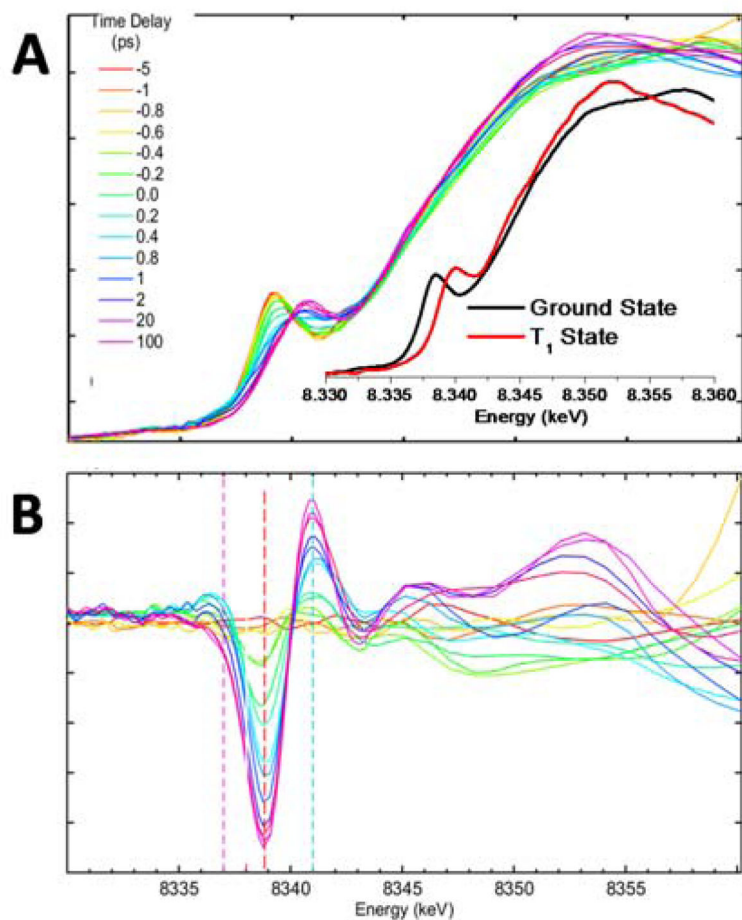
Figure 2.
A. Ni K-edge XANES spectra of NiTMP obtained at the LCLS at different time delays and at APS (inset) for the ground and T state (~100 ps delay limited by the APS pulse duration); B. difference XANES spectra with three dashed lines aligned with three X-ray photon energies at which the kinetic curves were collected.
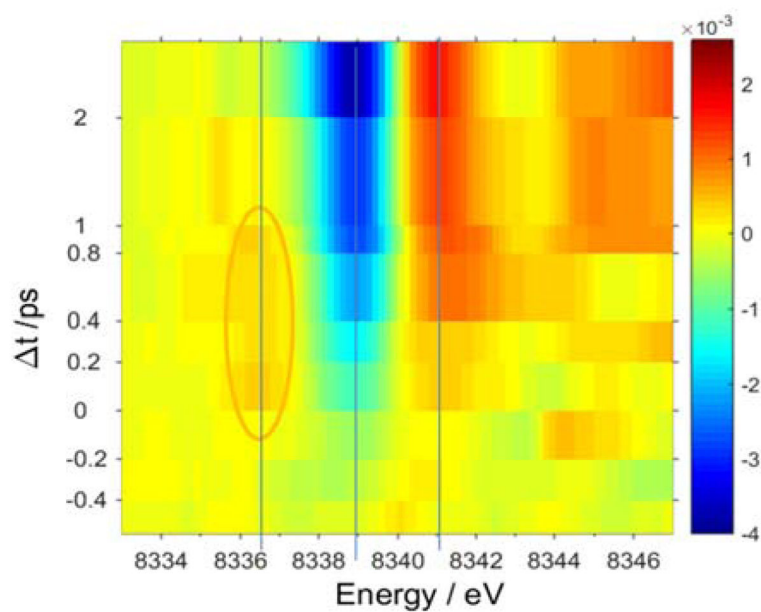
Figure 3.
The local contour plot of the difference spectra shown in Figure 2B where the three lines mark the energies where the kinetics data are obtained. The orange patch at 8337 eV suggests the rise and decay of a transient state within ~ 2ps of the excitation.
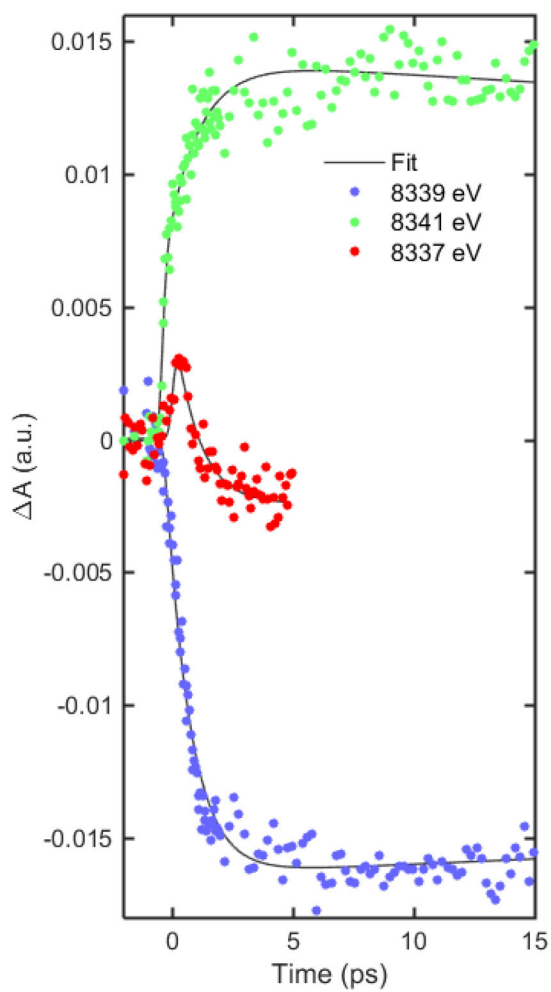
Figure 4.
Kinetics curves taken at the three X-ray photon energies as labelled by the vertical lines in Figures 2 and 3.
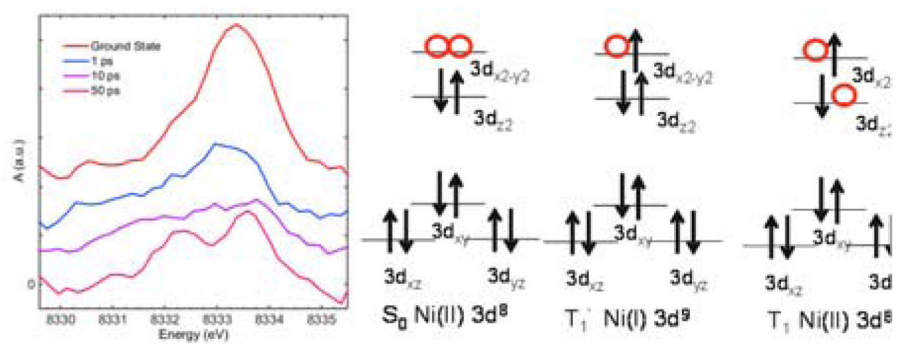
Figure 5.
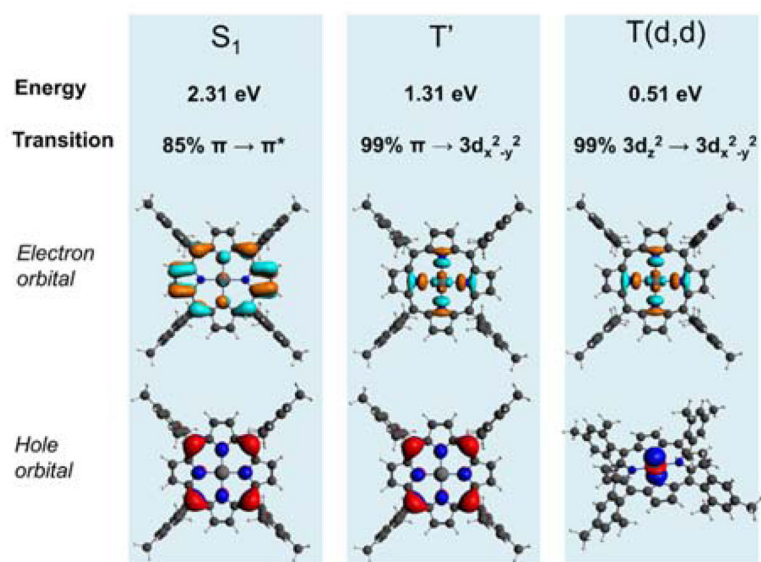The time evolution of the pre-edge 1s to 3d transition features.

Figure 6.
Molecular orbitals involved in each excited electronic state transition. Many features of the excited state XANES can be explained based on the movement of electron density on or off of the metal center.

Table 1

Orbital energies for the electronic ground state and changes in those energies in various excited states

		Inputs for excited-state XAS modeling					
Wave function[1]		S_0	$S_1(\pi,\pi^*)$	T'	$T(d,d)$	S_0	S_0
Geometry[2]		S_0	$S_1(\pi,\pi^*)$	T'	$T(d,d)$	T'	$T(d,d)$
		Calculated Ni orbital energies					
	eV	----------------------------		eV		----------------------------	
1s α	−8167.47	−0.05	2.02	−1.17	−0.37	−0.34
1s β	−8167.47	−0.05	2.03	−1.17	−0.37	−0.34
$4p_z$ α	1.39	−0.07	0.18	−0.23	−0.06	−0.03
$4p_z$ β	1.39	−0.06	0.05	−0.44	−0.06	−0.03